# Numerical simulation of the particle wall mass transfer rates on rough surfaces confining turbulent natural convection flows

Jordi Pallares* and Alexandre Fabregat

Departament d'Enginyeria Mecànica. Universitat Rovira i Virgili.

Av. Països Catalans, 26. 43007-Tarragona. Spain

*Corresponding author: jordi.pallares@urv.cat

Keywords: particle deposition; rough surfaces; turbulent natural convection; mass transfer; thermophoresis; cubical cavity

## ABSTRACT

We performed numerical simulations of the particle mass transfer rates on the horizontal and vertical thermally active rough walls confining a turbulent natural convection flow. We considered the air flow conditions in a cubical cavity ($L = 1.22\ m$, $Ra = 5.4 \cdot 10^8$, $Pr = 0.71$) with two opposed pairs of consecutive walls at different temperatures, for which measurements of the particle deposition velocities are reported in the literature. The simulations were carried out by solving the momentum, thermal energy and particle mass transfer equations using a series of two-dimensional computational cell units to determine spatial evolution and development of the particle concentration boundary layer in the vicinity of hot and cold rough walls. Different flow conditions, wall orientations, sizes of roughness elements, particle diameters and temperature increments between the wall and the bulk fluid, typically found in indoor environments, have been considered. At large mass transfer particle Péclet numbers, corresponding to spherical particles with diameters of 0.5-1 μm, the wall mass transfer rates of particles on rough textures typically increase by a factor of about 3 in comparison with the deposition on smooth surfaces. The thermophoretic effect significantly decreases the particle deposition on hot surfaces and increases it on cold surfaces, especially at large particle Péclet numbers. The numerical predictions of

the deposition velocities are in good agreement with the measurements reported in the literature for the same flow conditions considered.

## NOMENCLATURE

| | |
|---|---|
| $c$ | Concentration [kg m$^{-3}$] |
| $C_D$ | Drag coefficient [-] |
| $C_c$ | Cunningham slip correction factor [-] |
| $d$ | Size of the roughness element [m] |
| $d_p$ | Particle diameter [m] |
| $D$ | Diffusion coefficient [m$^2$ s$^{-1}$] |
| $g$ | Gravity acceleration [m s$^{-2}$] |
| $h$ | Height of the computational domain [m] |
| $k$ | Thermal conductivity [W m$^{-1}$ K$^{-1}$] |
| $k_B$ | Boltzmann constant [J K$^{-1}$] |
| $k_c$ | Convection mass transfer coefficient [m s$^{-1}$] |
| $Kn$ | Knudsen number ($Kn = 2\,\lambda/d_p$) [-] |
| $K_{TP}$ | Thermophoresis constant [-] |
| $L$ | Length of the cubical cavity [m] |
| $L_w$ | Length of the surface [m] |
| $n$ | Coordinate perpendicular to the wall [m] |
| $p$ | Pressure |
| $Pe$ | Mass transfer Péclet number ($Pe = Re_d Sc$) |
| $Pr$ | Prandtl number ($Pr = \nu/\alpha$) [-] |
| $Ra$ | Rayleigh number ($Ra = g\beta\Delta T L^3/\nu\alpha$) [-] |
| $Re$ | Reynolds number ($Re = U_\infty L/\nu$) [-] |
| $Re_d$ | Reynolds number ($Re_d = S_u d^2/\nu$) [-] |
| $Re_p$ | Particle Reynolds number ($Re = \left\|U_p - U_f\right\| d_p/\nu$) [-] |
| $Sc$ | Schmidt number ($Sc = \nu/D$) [-] |
| $Sh$ | Sherwood number ($Sh = k_c d/D$) [-] |
| $S_T$ | Temperature gradient [K m$^{-1}$] |
| $S_u$ | Shear rate [s$^{-1}$] |
| $t$ | Time [s] |

| | | |
|---|---|---|
| $T$ | Temperature [K] |
| $u, v$ | Velocity components [m $s^{-1}$] |
| $U$ | Velocity magnitude [m $s^{-1}$] |
| $x, y$ | Cartesian coordinates [m] |
| *Greek letters* | |
| $\alpha$ | Thermal diffusivity [$m^2 \cdot s^{-1}$] |
| $\beta$ | Thermal expansion coefficient [$K^{-1}$] |
| $\delta$ | Boundary layer thickness [m] |
| $\Delta$ | Increment [-] |
| $\lambda$ | Mean free path [m] |
| $\mu$ | Dynamic viscosity [$kg \cdot m^{-1}\ s^{-1}$] |
| $\nu$ | Kinematic viscosity [$m^2 \cdot s^{-1}$] |
| $\rho$ | Density [$kg \cdot m^{-3}$] |
| $\tau$ | Time scale [s] |
| $\upsilon$ | Deposition velocity [m $s^{-1}$] |
| *Subscripts* | |
| $\infty$ | Value outside the boundary layer |
| $C$ | Cold |
| $f$ | Fluid |
| $g$ | Gravitational settling |
| $h$ | Horizontal |
| $H$ | Hot |
| $in$ | Inlet |
| $l$ | Linear |
| $p$ | Particle |
| $s$ | Settling |
| $v$ | Vertical |
| $w$ | Wall |
| *Subscripts* | |
| $*$ | Non-dimensional |
| *Special symbols* | |
| $\langle\ \rangle$ | Surface averaged |

## 1. INTRODUCTION

Solid particle deposition onto surfaces holds significant relevance in numerous industrial, technological, environmental, and medical applications. Examples of such applications can be found in various fields such as the semiconductor industry (Simard-Normandin, 2020), multiphase chemical reactors (Boccardo et al., 2019), indoor air quality (Inthavong, 2020), soiling of artworks (Grau-Bové et al., 2019), and drug delivery through dry powder inhalers (Shahin and Chablani, 2023).

In particular, the deposition of particles on both smooth and rough surfaces within ducts and channels under forced convection air flows bears significant implications in the aforementioned applications. Researchers including Zhao and Wu (2006), Dritselis (2017), Wang et al. (2019), Hong et al. (2020) have numerically examined this flow configuration, while Hahn et al. (1985), Kvasnak et al. (1993), and Chavez et al. (2020) have conducted experimental studies. These investigations aimed to analyze the impact of rough elements' geometry on particle interception and deposition. Collectively, these studies consistently demonstrate an overall increase in particle deposition rates on rough surfaces when compared to smooth surfaces.

The removal rate of particles by deposition is also important to predict the decay of bulk concentration which, in turn, is key to assess the health risk due to particle inhalation. (Abadie et al. 2001, Lai, 2002). The deposition rate of aerosol particles is usually experimentally determined by monitoring the concentrations of airborne aerosol particles or by measuring the amount of deposited particles on sample surfaces installed on the walls adjacent to particle laden flows. Table I summarizes some of the experimental studies analyzing particle deposition on rough surfaces using test chambers. The existing studies in the field have predominantly focused on conducting experiments within chambers under forced convection conditions created by fans. In contrast, only Kalilainen et al. (2016) and Thatcher and Nazaroff (1997) reported measurements of particle deposition under controlled natural convection flows for smooth and rough surfaces respectively.

| Reference | Chamber dimensions (m)* | Roughness height (microns) | Roughness shape | Particle diameters (microns) | Surface orientation | Heat transfer | Flow |
|---|---|---|---|---|---|---|---|
| Shimada et al. (1988) | Cylinder Diameter 0.15 Height 0.15 | 64-201 | Stainless steel with structured roughness, Sandpaper | 0.01-0.18 | Sidewall | Isothermal | Fan |
| Thatcher and Nazaroff (1997) | 1.22 x 1.22 x 1.22 | 10, 180, 2400 | Scratched, dry wall texture, balls | 0.1, 0.5, 1.3 | Sidewalls, ceiling and floor | Hot sidewall and floor. Cold sidewall and ceiling | Natural convection |
| | 4.9 x 3 x 2.4 | 10, 180, 2400 | Scratched, dry wall texture, balls | 0.2, 1 | Hot and cold sidewalls | Hot and cold sidewalls | Natural convection |
| Abadie et al. (2001) | 0.6 x 0.6 x 0.6 | 0.3-50.8 | Wall papers, carpet, wood | 0.7-5 | Sidewalls, ceiling and floor | Isothermal | Fan |
| Lai et al. (2002) | 2 x 2 x 2 | Smooth, 2000 | Smooth Perspex, Structured roughness | 0.7-5.4 | Sidewalls | Isothermal | Fan |
| Lai and Nazzaroff (2005) | 1.22 1x 1.22 x 1.22 | 10, 70, 100, 150, 250 | Glass and sandpaper | 0.9-9.1 | Sidewalls | Isothermal | Fan |
| Hamdani et al. (2008) | 0.5 x 0.5 x 0.5 | 1.5-26 | Vinyl, wallpapers, wood, wall-plaster and concrete | 0.35-2 | Sidewalls | Isothermal | Fan |
| Hussein et al. (2009) | 1 x 1 x 1 | 47-368 | Wall papers, wall-plasters, carpets | 0.02-5 | Sidewalls, ceiling and floor | Isothermal | Fan |
| Kalilainen et al. (2016) | 0.7 x 0.7 x 0.7 | Smooth | - | 1, 2.5 | - | Hot and cold sidewalls | Natural convection |
| Wang et al. (2018) | 0.8 x 0.8 x 0.8 | 64-198 | textile materials | 0.37-1.6 | Sidewalls | Isothermal | Fan |
| Zhong et al. (2021) | 0.3 x 0.3 x 0.3 | 500 | 3D printed rectangular, triangular, semi-circular ribs | 0.3-5 | Floor | Isothermal | Fan |

(*) Length x width x height

Table I. Summary of experimental studies analyzing particle deposition on rough surfaces installed on the walls of chambers.

Indoor natural convection flows produced by different temperatures of the confining walls are typically encountered in poorly or unventilated spaces. Under these flow conditions, with relatively low velocities in the bulk of the fluid and relatively large

134 temperature gradients near the thermally active walls, the deposition of particles
135 depends strongly on the orientation of the wall, favoring, because of gravity, the
136 landing of particles, with relatively large inertia, on horizontal surfaces facing up.
137 Another effect that can strongly influence the particle deposition rates on the
138 thermally active walls is the thermophoretic effect, which enhances the particle mass
139 flux toward cold walls and decreases it on hot walls (see for example Michaelides,
140 2006). This relatively complex scenario, involving gravitational, thermophoretic and
141 Brownian forces acting on the particles, can be further complicated by the effect of the
142 surface roughness elements, which are known to generally enhance the particle
143 deposition on the walls for forced convection conditions.
144
145 The objective of this study is to analyze the effect of the surface roughness elements
146 on the particle deposition rates on the thermally active walls of a confined turbulent
147 natural convection flow and contribute to improve our current limited understanding
148 of this flow configuration that has important implications for indoor air quality and
149 valuable surface soiling. We report numerical simulations for different particle
150 diameters, roughness sizes, surface orientations and wall-to-fluid temperature
151 increments, typically found in indoor environments and exhibition cases of artwork.
152

## 2. PHYSICAL MODEL

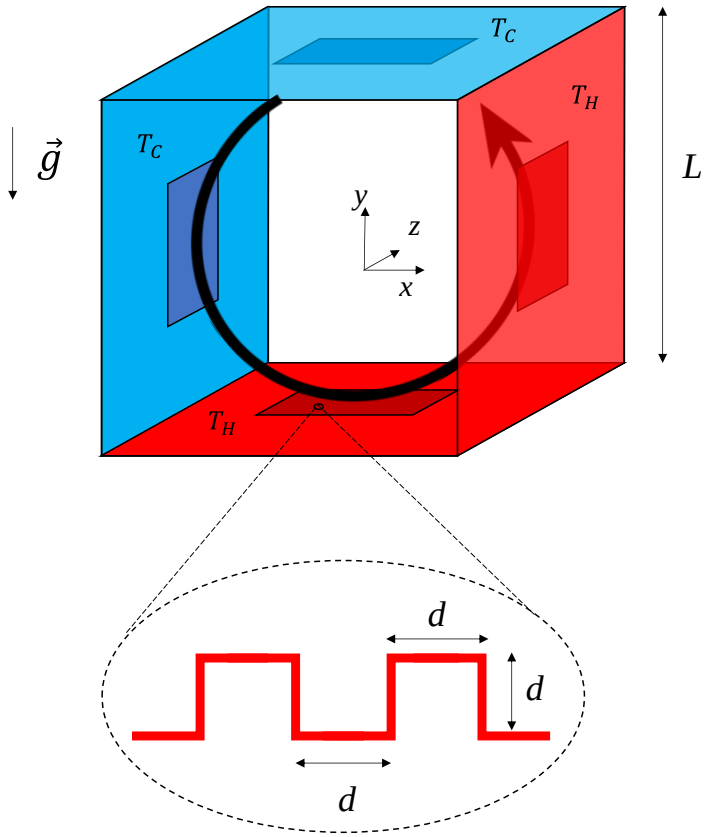


Figure 1. Physical model

Figure 1 shows a sketch of the cubical cavity used in the experiments of Thatcher and Nazaroff (1997), who measured particle deposition rates on rough surfaces using this natural convection flow configuration. The flow is driven by heating, at constant temperature $T_H$, the bottom wall and a vertical wall. The two opposite horizontal and vertical walls are kept at a lower temperature, $T_C$. The remaining two vertical walls are considered adiabatic. The flow at high Rayleigh numbers ($Ra \sim 10^8$) consists, essentially, in a turbulent large-scale flow circulation and thin laminar boundary layers attached to the thermally active walls (Fabregat and Pallares, 2020). In this study we consider the particle deposition on rough surfaces installed on the central part of the horizontal and vertical isothermal walls, mimicking the experimental arrangement by Thatcher and Nazaroff (1997). The roughness elements are assumed to be two dimensional with a square cross section (see Fig. 1).

As reported by Lai and Nazaroff (2005) the typical sizes of the small wall roughness elements ($d$) found indoors range between 70 μm and 250 μm. These sizes are three to four orders of magnitude smaller than the typical sizes of display cases of artworks or indoor environments ($L{\sim}1m$). This relatively large ratio between length scales ($L/d{\sim}10^4 - 10^3$) allows us to assume that the development of the mass transfer boundary layer over a distance equal to a few hundred roughness elements occurs essentially under constant velocity and temperature profiles. To simulate the mass transfer boundary layer over a surface covered by a large number of roughness elements we considered a series of unit computational cells constituted by two consecutive roughness elements. The computational strategy consists of sequentially solving the concentration field in a unit computational cell using the outflow concentration profile as the inflow boundary condition in the next downstream cell. Compared to a single computational domain consisting of the totality of the roughness elements, this strategy allows a significant reduction in computational costs. The procedure of these sequential simulations is described in detail in the next section where the computational aspects of the problem are discussed.

Direct Numerical Simulation (DNS) of the turbulent flow at $Ra = 5.4 \cdot 10^8$ and $Pr = 0.71$ in this flow configuration ($L = 1.22\ m$) revealed that the distance from the wall for which the velocity and thermal boundary layers have a constant gradient (i.e. linear profiles) is about $\delta_l \approx 0.01\ L$ (see Figs. 13 and 14 of Fabregat and Pallares, 2020). This simulation also indicates that the boundary layers near the vertical and horizontal walls are laminar and essentially steady, with relatively small fluctuations intensities. Consequently, the ratio between the thickness of these layers, characterized by linear velocity and temperature profiles, and the typical size of the roughness elements ($70\ \mu m \leq d \leq 250\ \mu m$) ranges between 170 and 50 for the smallest and largest elements, respectively. Under these conditions, and taking into account the large Schmidt number ($Sc{\sim}10^4 - 10^6$) of the particles based on the Brownian diffusion coefficient, it is reasonable to consider that the particle mass transfer boundary layer develops within a region of constant velocity and temperature gradients (i.e. with linear velocity and temperature profiles). We denote this constant shear rate as, $S_u$ and the constant temperature gradient as $S_T$.

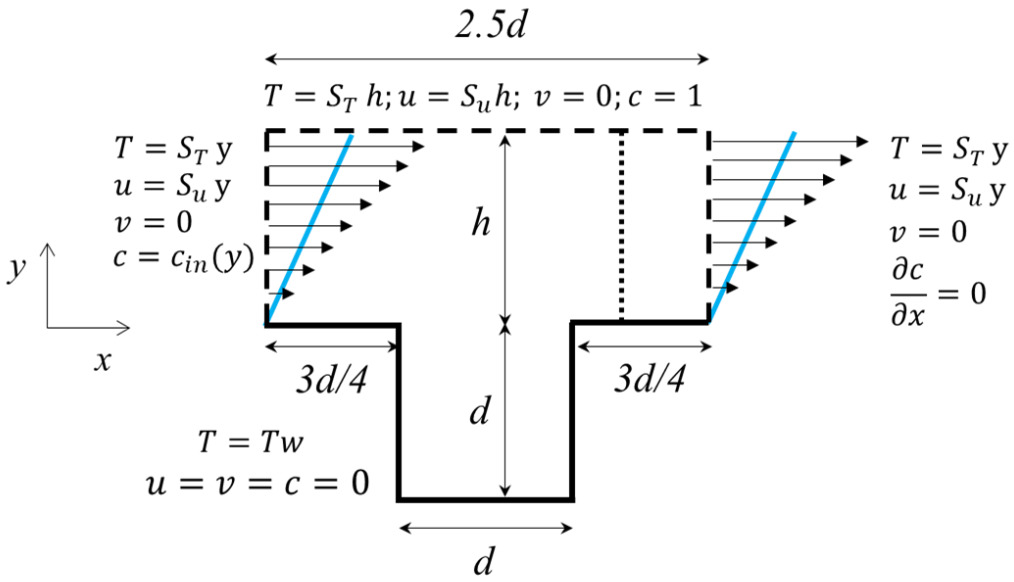


Figure 2. Computational domain and boundary conditions.

According to these hypotheses, the two-dimensional physical domain considered for the simulations is shown in Fig. 2. Non-slip and constant and uniform temperature boundary conditions are imposed at the bottom boundary of the domain. In this wall, the concentration of the particles is set to zero according to the assumption of a perfect sink for particles (i.e. no rebound and no particle resuspension). At the inlet and outlet boundaries constant linear velocity and temperature profiles are considered. For the concentration we impose a known vertical concentration profile at the inlet and outflow conditions at the outlet. The mathematical details of these boundary conditions are given in next section. The top boundary, located at a distance ($h$) from the top of the roughness elements, is considered to be far enough from the edge mass transfer boundary to impose constant and uniform velocity, temperature and concentration.

## 3. MATHEMATICAL MODEL

### *3.1. Governing equations*

Considering constant physical properties and steady flow conditions within the two-dimensional boundary layer, the non-dimensional continuity, momentum and thermal energy equations can be written as

$$\frac{\partial u_i^*}{\partial x_i^*} = 0, \tag{1}$$

$$\frac{\partial u_j^* u_i^*}{\partial x_j^*} = -\frac{\partial p^*}{\partial x_i^*} + \frac{1}{Re_d}\frac{\partial^2 u_i^*}{\partial x_j^{*2}} \tag{2}$$

and

$$\frac{\partial u_j^* T^*}{\partial x_j^*} = \frac{1}{Re_d\, Pr}\frac{\partial^2 T^*}{\partial x_j^{*2}}. \tag{3}$$

The time and length scales, used to obtain the non-dimensional variables, are the inverse of the shear rate $S_u$ and the height of the roughness elements, $d$, consequently the velocity scale is $d/S_u$. In Eq. 3, $Re_d = S_u d^2/\nu$ is the Reynolds number and $Pr = \nu/\alpha$ is the Prandtl number. The non-dimensional temperature is defined as $T^* = (T - T_\infty)/|T_w - T_\infty|$. Note that according to this definition $T^* = 1$ at the hot wall ($T_w > T_\infty$) and $T^* = -1$ at the cold wall ($T_w < T_\infty$).

The non-dimensional mass transfer equation that governs the steady state two-dimensional spatial distribution of the concentration of particles can be expressed as,

$$\frac{\partial u_{pi}^* c^*}{\partial x_i^*} = \frac{1}{Re_d\, Sc}\frac{\partial^2 c^*}{\partial x_i^{*2}}. \tag{4}$$

In Eq. 4, $u_{pi}^{*}$ is the non-dimensional particle velocity and $Sc = \nu/D$ is the Schmidt number. The diffusion coefficient of the particles, $D$, is computed with the Stokes-Einstein equation for spherical particles

$$D = k_B T_w C_c / 3\pi\mu d_p. \quad (5)$$

In Eq. 5, $C_c$ is the Cunningham factor, which can be expressed as a function of the Knudsen number ($Kn = 2\,\lambda/d_p$) as (Allen and Raabe, 1982)

$$C_c = 1 + Kn[1.205\ exp(-0.0026/Kn) + 0.425\ \exp\ (-0.74/Kn)]. \quad (6)$$

Considering the dilute approximation (i.e. no interaction between particles and particles do not influence the fluid velocity), the local particle velocity is governed by the second Newton's law, which for $Re_p < 1$, ($C_D = 24/Re_p$ i.e. small spherical particles in creeping flow) can be written as

$$\frac{d\vec{v}_p}{dt} = \frac{(\vec{v}-\vec{v}_p)}{\tau_p} + \left(1 - \frac{\rho}{\rho_p}\right)\vec{g} - \frac{18\mu^2 C_c}{\rho\ \rho_p\ d_p^2} K_{tp} \frac{\vec{\nabla} T}{T_\infty}. \quad (7)$$

The different terms on the right-hand side of Equation 7 are, from left to right, the hydrodynamic drag force, the gravity force and the thermophoretic force. The accelerations originated from the pressure gradient force, the added mass force, the Basset force and the lift force, which are proportional to the ratio between the fluid density and the particle density are neglected in Eq. 7 since, for solid gas flows, $O(\rho/\rho_p) \sim 10^{-3}$. In Eq. 7, $\tau_p$ is the particle relaxation time defined in Eq. 8.

$$\tau_p = \frac{\rho_p d_p^2}{18\mu C_c} \quad (8)$$

The value of $K_{tp}$ in the thermophoretic force (see Eq. 7), for $Kn > 0.1$, can be computed as (Talbot et al. 1980)

$$K_{tp} = \frac{2C_s(k+2k_p Kn)\left[1+2Kn\left(1.2+0.41\ exp(-0.44/Kn)\right)\right]}{(1+6C_m Kn)(2k+k_p+4k_p C_t Kn)}, \quad (9)$$

with $C_s = 1.17$, $C_m = 1.14$ and $C_t = 2.18$.

Assuming small particles ($Re_p < 1$) and slow time varying fluid velocities near the wall, within the laminar boundary layer, we can neglect the acceleration term on the left-hand side of Eq. 7 and the non-dimensional velocity of the particle can be computed as

$$u_{pi}^* = u_i^* + \left(1 - \frac{\rho}{\rho_p}\right)\frac{\tau_p g_i}{S_u\, d} - \frac{K_{tp}}{Re_d}\left|\frac{T_w}{T_\infty} - 1\right|\frac{\partial T^*}{\partial x_i^*}. \quad (10)$$

In Equation 10, the different terms on the right-hand side are, from left to right, the fluid velocity, the non-dimensional settling velocity, $V_{si}^* = \left(1 - \frac{\rho}{\rho_p}\right)\frac{\tau_p g_i}{S_u\, d}$, and the thermophoretic velocity. The constant settling velocity can be absorbed into the fluid velocity, ($\tilde{u}_i^* = u_i^* + V_{si}^*$, see for example Pallares and Fabregat, 2020).

$$u_{pi}^* = \tilde{u}_i^* - \frac{K_{tp}}{Re_d}\left|\frac{T_w}{T_\infty} - 1\right|\frac{\partial T^*}{\partial x_i^*}. \quad (11)$$

The introduction of the particle velocity (Eq. 11) into Eq. 4 results in

$$\tilde{u}_i^*\frac{\partial\, c^*}{\partial x_i^*} = \frac{K_{tp}}{Re_d}\left|\frac{T_w}{T_\infty} - 1\right|\frac{\partial}{\partial x_i^*}\left(c^*\frac{\partial T^*}{\partial x_i^*}\right) + \frac{1}{Re_d\, Sc}\frac{\partial^2 c^*}{\partial x_i^{*2}}. \quad (12)$$

Equation (12) is the non-dimensional mass transfer equation as a function of the local fluid velocities and temperatures.

*3.2. Boundary conditions and computational model*

According to the hypotheses described above, Equations 1, 2, 3 and 12 constitute the set of governing equations of the problem. The solution of these equations, together with the corresponding boundary conditions, has been obtained sequentially in a series of concatenated computational cells. The computational unit cell is shown in Fig. 2. The boundary conditions are indicated in this figure. For given values of the

Reynolds number and of the temperature gradient, the velocity and the temperature distribution are the same in all the computational cells, according to the fully developed assumption for velocity and temperature. At the first computational cell we impose $c^* = 1$ at the inlet of the domain and zero diffusion flux at the outlet (see Fig. 2). Once the concentration field is converged in the first computational cell, the concentration profile at $x^* = 2$, indicated in Fig. 2 with a dotted vertical line, is used as inlet boundary conditions for the second computational cell. This procedure is repeated sequentially for 1000 computational cells. The streamwise extension of the computational cell is $L_x^* = 2.5$ (see Fig. 2) and the concentration profile to be imposed to the next computational cell is taken at $x^* = 2$ to minimize the effect of the outlet boundary condition for concentration on the concentration distribution at the inlet of the next computational cell.

Equations 1, 2, 3 and 12 and the corresponding boundary conditions were solved numerically with the second-order accuracy finite volume code 3DINAMICS. For the momentum and thermal energy equations the discretization of the convective terms is centered and for the mass transfer equation is based on the TVD scheme (Koren, 1993), which avoids the non-physical wiggles that appear at large Péclet numbers produced by the centered scheme. The diffusion terms of all equations are discretized with the centered second order scheme. This code has been used successfully for the simulation of mass transfer boundary layer flows (Pallares and Grau 2014, Pallares and Ferré 2015, Pallares 2015) and of convection heat transfer in porous media using the unit cell scale approach (Pallares and Grau, 2010).

To select the grid resolution, we performed a simulation in the first computational cell, which is the one with the largest concentration gradients, using three different meshes at the largest Péclet number considered ($Pe = Re_d Sc \approx 3 \cdot 10^4$). All the grids have the nodes stretched towards the walls. The computational cell has dimensions 2.5x17 ($h = 16\ d$, see Fig. 2). This vertical dimension is larger than the mass transfer boundary layer thickness at the last computational cell for the lowest Péclet number considered ($Pe \approx 26$). The coarse grid (grid 1) has 73x218 grid points, the medium grid, 143x368 grid points and the fine grid, 187x434 grid points. Figure 3 shows the numerical

predictions of the local Sherwood number ($Sh = \left.\frac{\partial c^*}{\partial n^*}\right|_w$) along the wall for the three meshes. It can be seen that grid 2 and grid 3 give very similar results. The difference between the surface averaged Sherwood numbers of these two grids is about 1% for these extreme conditions (i.e. largest Péclet number and first computational cell) corresponding to the largest Sherwood numbers. According to this, grid 2 has been selected for the simulations.

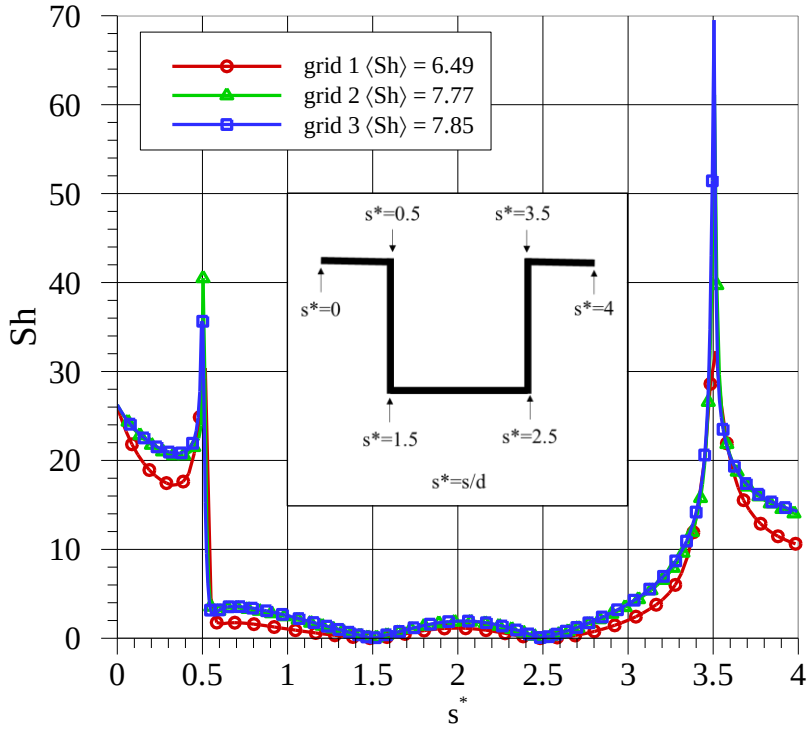


Figure 3. Grid independence test. Local Sherwood number along the wall. Surface averaged values are indicated in the legend.

*3.3. Parameters of the simulations*

Table II indicates the parameters of the experimental flow configuration used by Thatcher et al. (1996) and Thatcher and Nazaroff (1997) to carry out the measurements of particle deposition on smooth and rough horizontal and vertical surfaces produced by a confined turbulent natural convection of air using the flow configuration shown in Fig. 1. We included in Table II, the Reynolds number, the non-dimensional wall shear rates [$S_u^* = (L/U_\infty)(\partial u/\partial y)$] and the temperature gradients

355 $[S_T^* = (2L/\Delta T)(\partial T/\partial y)]$ at the center ($x/L = 0.5$) of the horizontal ($S_{uh}^*$ and $S_{Th}^*$) and
356 vertical ($S_{uv}^*$, $S_{Tv}^*$) walls computed from the DNS of Fabregat and Pallares (2020). Note
357 that the temperature scale is half of the temperature increment between the hot and
358 cold walls (i.e. $\Delta T = T_H - T_C$; $|T_w - T_\infty| = \Delta T/2$).
359

| $L$ (m) | $\Delta T$ (K) | $Ra$ | $Pr$ | $Re$ $U_\infty L/\nu$ | $S_{uh}^*, S_{uv}^*$ $\frac{x}{L} = 0.5$ | $S_{Th}^*, S_{Tv}^*$ $\frac{x}{L} = 0.5$ |
|---|---|---|---|---|---|---|
| 1.22 | 3 | $5.4 \cdot 10^8$ | 0.70 | 6640 | 53.2, 143.9 | -38.3, -45.9 |

360 Table II. Non-dimensional numbers corresponding to the experimental conditions of
361 Thatcher and Nazaroff (1997).
362
363 Table III summarizes the ranges of the different parameters of the particles considered
364 for the simulations. The physical properties and sizes of the particles correspond to the
365 ammonium fluorescein particles used by Thatcher and Nazaroff (1997) in their
366 measurements of particle deposition on rough surfaces. These rough surfaces with
367 length $L_w = 0.1\ m$ and width 0.3 m were installed on the central part of the horizontal
368 and vertical thermally active walls of a test chamber as depicted in Fig. 1.
369

| $d_p$ (μm) | $\rho_p$ (kg/m$^3$) | $k_p$ (W/m·K) | $K_{tp}$ | $Kn$ | $C_c$ | $D$ (m$^2$/s) | $Sc$ |
|---|---|---|---|---|---|---|---|
| 0.1 | 1350 | 0.430 | 0.247 | 1.36 | 2.97 | $6.69 \cdot 10^{-10}$ | $2.24 \cdot 10^4$ |
| 0.5 | | | 0.240 | 0.272 | 1.33 | $6.69 \cdot 10^{-11}$ | $2.50 \cdot 10^5$ |
| 1.3 | | | 0.227 | 0.105 | 1.12 | $1.95 \cdot 10^{-11}$ | $7.71 \cdot 10^5$ |

370 Table III. Physical parameters of the particles considered for the simulations.
371
372 We selected the minimum and maximum sizes of the typical roughness elements
373 found indoors according to Lai and Nazaroff (2005). ($d$=70 μm and $d$=250 μm) and the
374 size of the roughness elements ($d$=180 μm) used by Thatcher and Nazaroff (1997).
375 Table IV indicates the values of the Reynolds numbers based on the size of the

roughness elements and on the wall shear rate on the horizontal ($Re_{dh}$) and vertical ($Re_{dv}$) walls. The corresponding non-dimensional wall shear rates are also included.

| $d$ (μm) | $L/d$ | $Re_{dh}$ $S_{uh}d/\nu$ | $Re_{dv}$ $S_{uv}d/\nu$ | $S_{Th}^{**}$ $S_{Th}^{*}d/L$ | $S_{Tv}^{**}$ $S_{Tv}^{*}d/L$ |
|---|---|---|---|---|---|
| 70 | $1.74\cdot10^{4}$ | $1.16\cdot10^{-3}$ | $3.15\cdot10^{-3}$ | $-2.20\cdot10^{-3}$ | $-2.63\cdot10^{-3}$ |
| 180 | $6.78\cdot10^{3}$ | $7.69\cdot10^{-3}$ | $2.08\cdot10^{-2}$ | $-5.65\cdot10^{-3}$ | $-6.77\cdot10^{-3}$ |
| 250 | $4.88\cdot10^{3}$ | $1.48\cdot10^{-2}$ | $4.01\cdot10^{-2}$ | $-7.84\cdot10^{-3}$ | $-9.41\cdot10^{-3}$ |

Table IV. Non-dimensional numbers corresponding to different roughness sizes.

It can be seen that the typical Reynolds numbers range from, approximately, $10^{-3}$ to $5\cdot10^{-2}$ corresponding, respectively, to the smallest and largest roughness elements.

Table V summarizes the non-dimensional parameters of the governing equations (Eqs. 1-3 and 12) for the 60 different cases simulated. The simulations were carried out for four different Reynolds numbers, in the range of the values shown in Table IV, three different Schmidt numbers, corresponding the to the three different particle sizes indicated in Table IV, and five different wall-to-fluid temperature increments. Note that each case has been computed in 1000 unit cells and this corresponds to 60000 simulations in the computational domain of the unit cell shown in Fig. 2.

392

| | | | $\frac{K_{tp}}{Re_d}\left\lvert\frac{\Delta T_{1/2}}{T_\infty}\right\rvert$ | | |
|---|---|---|---|---|---|
| $Re_d$ | $Sc$ | $Pe$ | $\Delta T_{1/2}=0$ | $\Delta T_{1/2}=\pm 1.5$℃ | $\Delta T_{1/2}=\pm 3$℃ |
| $1.16\cdot10^{-3}$ | $2.24\cdot10^{4}$ | $2.60\cdot10^{1}$ | 0 | $1.06\cdot10^{0}$ | $2.12\cdot10^{0}$ |
| | $2.50\cdot10^{5}$ | $2.90\cdot10^{2}$ | | $1.03\cdot10^{0}$ | $2.07\cdot10^{0}$ |
| | $7.71\cdot10^{5}$ | $8.94\cdot10^{2}$ | | $9.74\cdot10^{-1}$ | $1.95\cdot10^{0}$ |
| $7.69\cdot10^{-3}$ | $2.24\cdot10^{4}$ | $1.72\cdot10^{2}$ | | $2.23\cdot10^{-1}$ | $4.46\cdot10^{-1}$ |
| | $2.50\cdot10^{5}$ | $1.92\cdot10^{3}$ | | $2.17\cdot10^{-1}$ | $4.34\cdot10^{-1}$ |
| | $7.71\cdot10^{5}$ | $5.93\cdot10^{3}$ | | $2.05\cdot10^{-1}$ | $4.10\cdot10^{-1}$ |
| $2.08\cdot10^{-2}$ | $2.24\cdot10^{4}$ | $4.66\cdot10^{2}$ | | $5.94\cdot10^{-2}$ | $1.19\cdot10^{-1}$ |
| | $2.50\cdot10^{5}$ | $5.20\cdot10^{3}$ | | $5.78\cdot10^{-2}$ | $1.16\cdot10^{-1}$ |
| | $7.71\cdot10^{5}$ | $1.60\cdot10^{4}$ | | $5.45\cdot10^{-2}$ | $1.09\cdot10^{-1}$ |
| $4.01\cdot10^{-2}$ | $2.24\cdot10^{4}$ | $8.98\cdot10^{2}$ | | $3.07\cdot10^{-2}$ | $6.15\cdot10^{-2}$ |
| | $2.50\cdot10^{5}$ | $1.00\cdot10^{4}$ | | $2.99\cdot10^{-2}$ | $5.99\cdot10^{-2}$ |
| | $7.71\cdot10^{5}$ | $3.09\cdot10^{4}$ | | $2.82\cdot10^{-2}$ | $5.65\cdot10^{-2}$ |

393 Table V. Simulated cases.

394

## 4. RESULTS AND DISCUSSION

### *4.1. Velocity and temperature distributions*

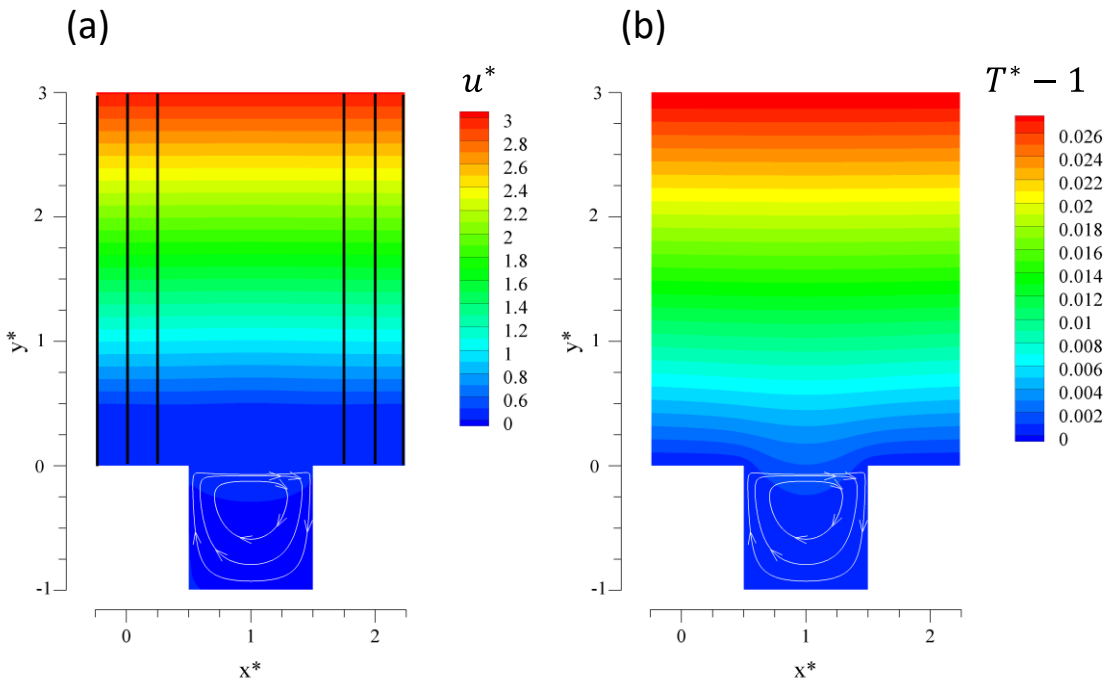


Figure 4. Velocity (a) and temperature (b) contours at $Re = 4.01 \cdot 10^{-2}$

As an example of the velocity and temperature distributions in a computational cell, Figure 4 shows contours of the parallel-to-the-wall velocity component (Fig. 4.a) and temperature (Fig. 4.b) at the largest Reynolds number considered ($Re = 4.01 \cdot 10^{-2}$) near a cold wall. Note that the extension of an individual computational cell is· $L_x^* \times L_y^* = 2.5 \times 17$ and consequently Figure 4 shows only the contours near the wall (i.e. for $y^* < 3$). The flow recirculation, depicted with streamlines in Figure 4, between two consecutive roughness elements is highly symmetric according to the creeping flow conditions (Re<<1). The temperature and velocity profiles along the vertical lines indicated in Figure 4.a are plotted in Figure 5. The lines are located at $x^* = -0.25, 0, 0.25, 1.75, 2$ and $2.25$.

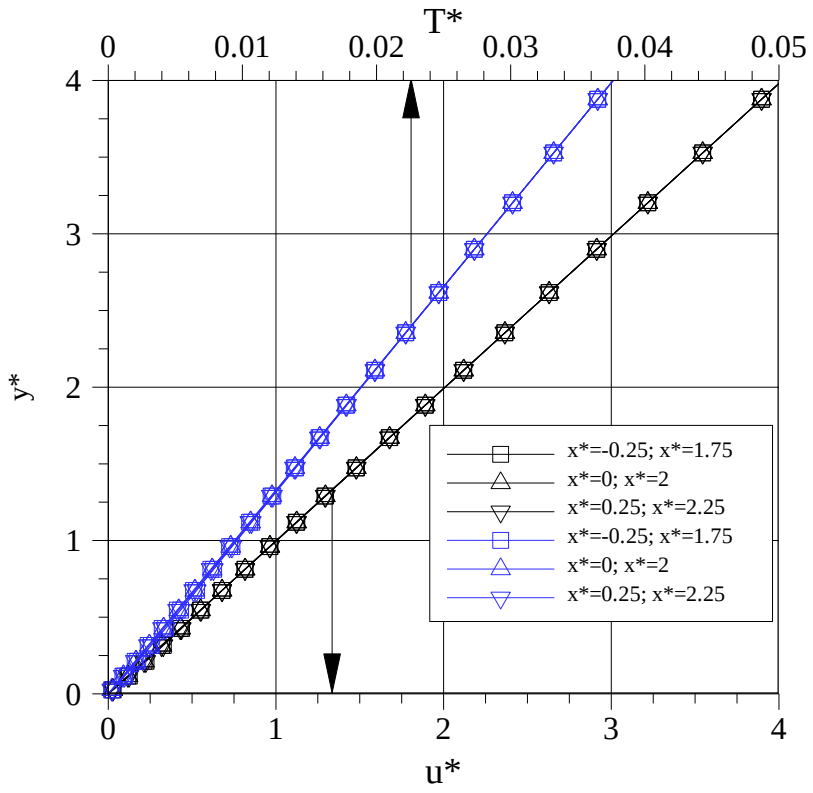


412

413 Figure 5. Non-dimensional temperature and x-velocity component along the lines
414 indicated in Fig. 4.a ($Re = 4.01 \cdot 10^{-2}$).

415

416 It can be seen that above the roughness elements the velocity and temperature
417 distributions exhibit a vertical linear profile irrespectively of the streamwise position.
418 Also, it is evident that at these low Reynolds numbers the distortion of the velocity and
419 temperature is located, near the wall, above the region between the roughness
420 elements.

421 Figure 6 shows, for reference, the non-dimensional particle concentration contours,
422 near the wall ($-1 < y^* < 3$) in the 10 first computational cells at $Pe = 2.60 \cdot 10^2$ (Fig.
423 6.a) and $Pe = 5.20 \cdot 10^3$ (Fig. 6.b). The effect of the Péclet number is evident when
424 comparing the mass transfer boundary layer thickness of the two cases depicted in this
425 figure.

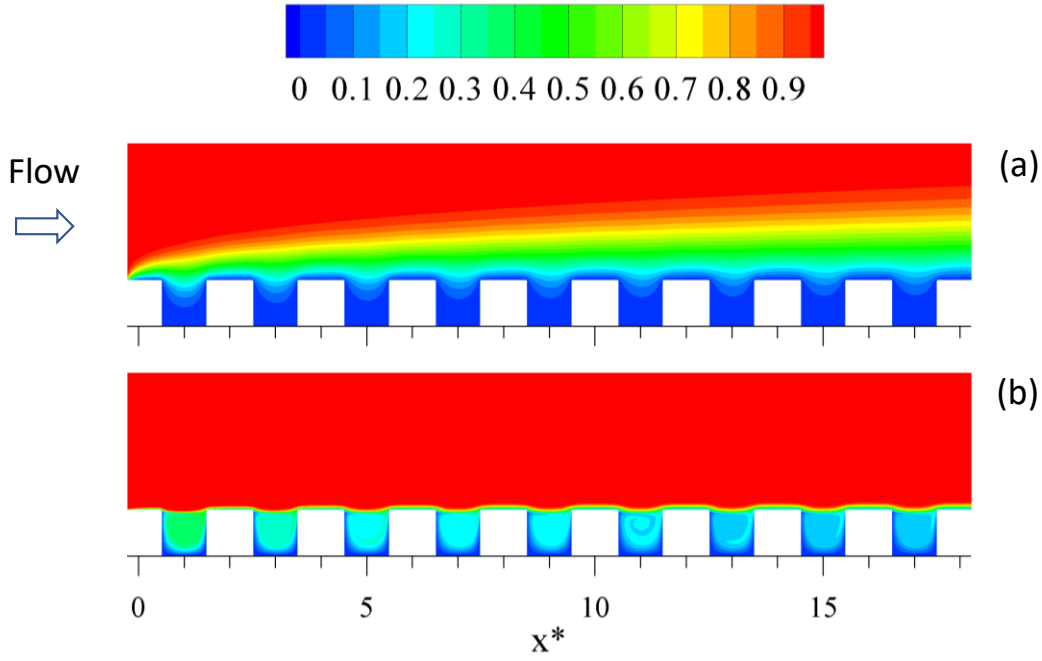


Figure 6. Non-dimensional particle concentration contours e and x-velocity at (a) $Pe = 2.60 \cdot 10^2$ and (b) $Pe = 5.20 \cdot 10^3$.

*4.2. Particle wall mass transfer rates and deposition velocities*

In this section we report the particle wall mass transfer rate for the cases considered in Table V. The definition of the local Sherwood numbers based on the local mass transfer coefficient and the length of the wall ($L_w$) or the dimension of the roughness elements ($d$) are

$$Sh_{L_w}(x) = \frac{k_c(x)L_w}{D}, Sh_d(x) = \frac{k_c(x)d}{D}, Sh_{L_w}(x) = Sh_d(x)\frac{L_w}{d} \quad (13)$$

The local Sherwood number, or the non-dimensional transfer rate, of a passive scalar from a smooth wall under a momentum boundary layer with a uniform and constant linear velocity profile can be predicted with the Lévêque solution (Lévêque, 1928).

$$Sh_{Lévêque}(x) = \frac{k_c(x)L_w}{D} = 0.5384\left(\frac{Re_d Sc}{x/d}\right)^{1/3}\frac{L_w}{d} \quad (14)$$

The corresponding surface averaged Sherwood can be written as

$$\langle Sh\rangle_{Lévêque} = \frac{\langle k_c\rangle L_w}{D} = 0.8075(Re_d Sc)^{1/3}\left(\frac{L_w}{d}\right)^{2/3} \quad (15)$$

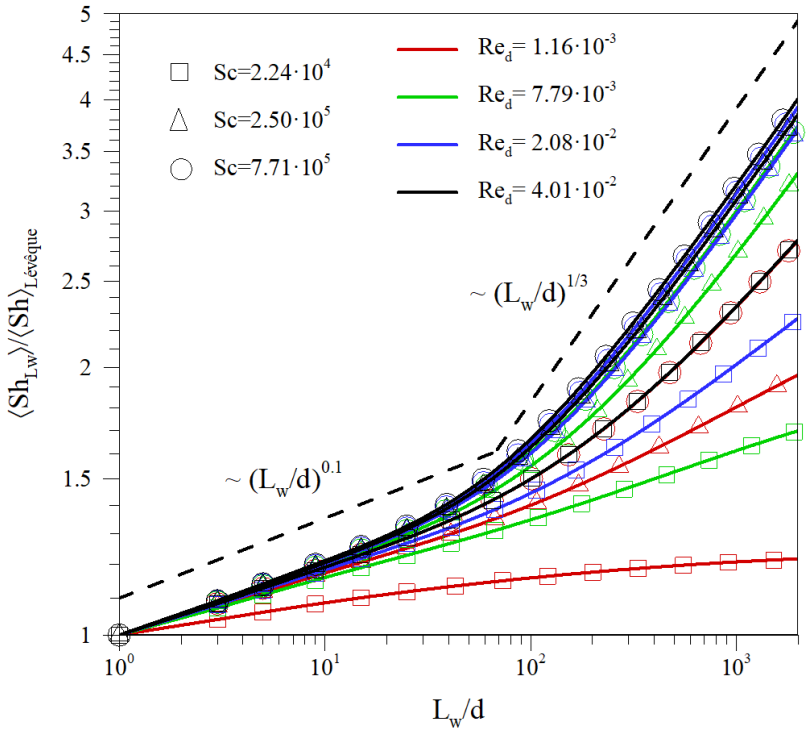


Figure 7. Surface averaged Sherwood number, scaled with the Sherwood number corresponding to the Lévêque solution (smooth wall), as a function of the length of the surface with the roughness elements.

Figure 7 shows the ratio of the numerically predicted surface averaged Sherwood number and the surface averaged Sherwood number of a smooth surface according to the analytical solution proposed by Lévêque (1928).

$$\frac{\langle Sh_{L_w}\rangle}{\langle Sh\rangle_{Lévêque}} = \frac{\langle Sh_d\rangle}{0.8075(Re_d Sc)^{1/3}\left(\frac{L_w}{d}\right)^{2/3}} \quad (16)$$

It can be seen that the roughness elements increase the wall mass transfer rates with respect to the smooth wall. The augmentation depends on the product of the Reynolds number and the Schmidt number or the Péclet number. Note for example that the cases $Re_d = 4.01 \cdot 10^{-2}$, $Sc = 2.24 \cdot 10^4$ (black squares) and $Re_d = 1.16 \cdot 10^{-3}$, $Sc = 7.71 \cdot 10^5$ (red circles) show almost coincident curves because of the very similar Péclet numbers ($Re_d Sc = 898.2$ and $894.4$, respectively). At high Péclet number ($Re_d Sc \to \infty$) the ratio of the Sherwood numbers increases with the one-third power of the length of the rough wall, for walls with lengths corresponding to more than approximately one hundred of roughness elements.

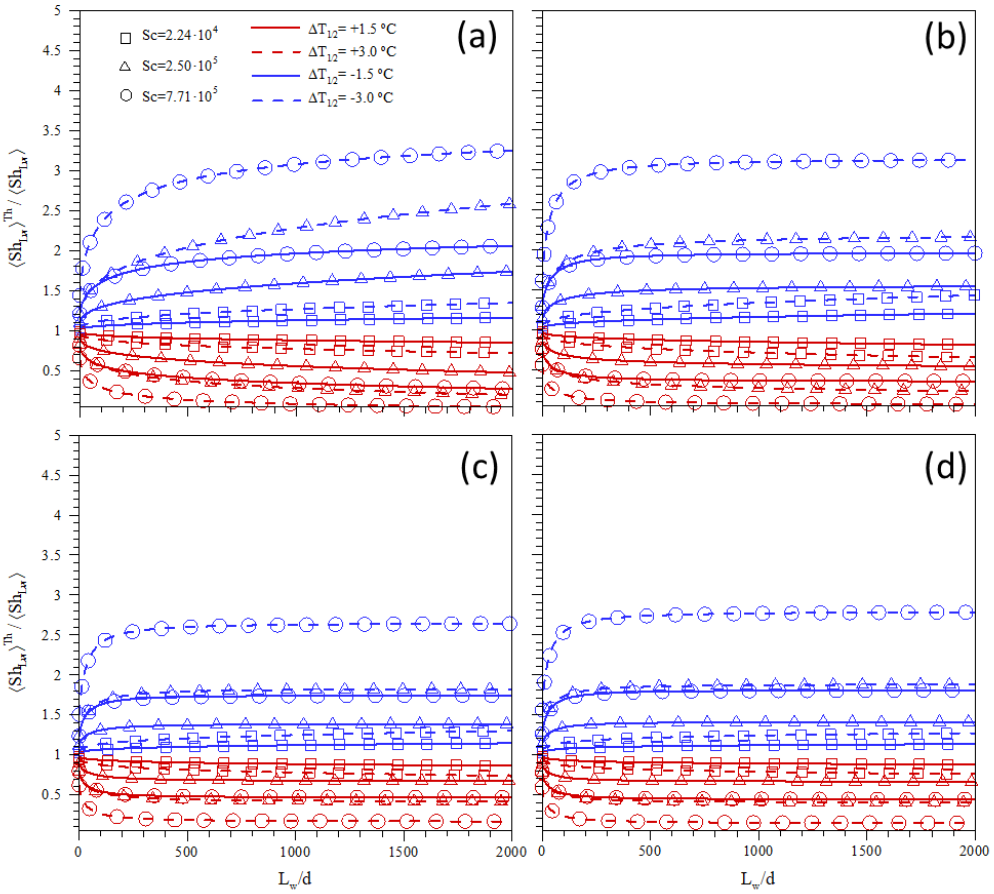


Figure 8. Surface averaged Sherwood number considering the thermophoretic effect, scaled with the Sherwood number corresponding to the isothermal case, as a function of the length of the surface with the roughness elements. (a) $Re_d = 1.16 \cdot 10^{-3}$, (b) $Re_d = 7.79 \cdot 10^{-3}$, (c) $Re_d = 2.08 \cdot 10^{-2}$, (d) $Re_d = 4.01 \cdot 10^{-2}$

The effect of thermophoresis on the surface averaged Sherwood number is shown in Figure 8. In this figure we plotted the ratio between the non-dimensional mass transfer rate considering thermophoresis and the Sherwood number of the isothermal case ($\langle Sh_L \rangle^{Th} / \langle Sh_L \rangle$) as a function of the length of the roughness wall. As expected, Figure 8 shows that the deposition is enhanced, with respect to the isothermal case, on rough cold walls (blue curves) and it is reduced on the hot walls (red curves). At high Reynolds numbers (Figs. 8c to 8d) the ratio of the surface averaged Sherwood numbers attains a constant value independently of the dimension of the rough wall for wall lengths larger than approximately a few hundreds of rough elements ($L_w/d \approx 500$). This ratio approximately corresponds to the size of one of the roughness elements ($d = 180\ \mu m$) and the length of the surface ($L_w = 0.1\ m$) used in the experiments of Thatcher and Nazaroff (1997) ($L_w/d = 555.6$). The increase of the deposition rate on cold walls is more evident at low Reynolds number and high Schmidt number. For example, at $Sc = 7.71 \cdot 10^5$, for a temperature increment of $\Delta T_{1/2} = -3.0°C$ and the lowest Reynolds number (Fig. 8a) the ratio of the Sherwood numbers is about 3 while for the highest Reynolds number (Fig. 8d) is reduced down to 2.6. At low Reynolds number and for the maximum temperature increment ($\Delta T_{1/2} = 3.0°C$), the deposition is essentially suppressed on the hot walls, especially for high Schmidt numbers.

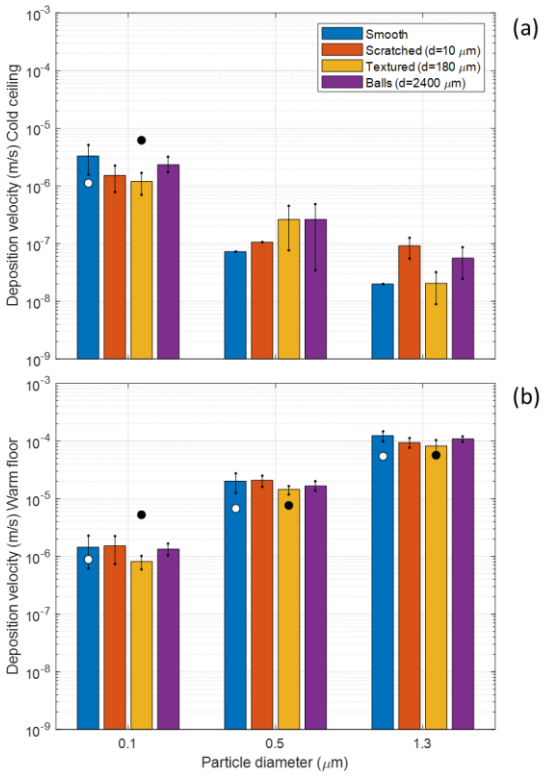


494

495 Figure 9. Deposition velocities on the (a) cold ceiling and (b) warm floor.

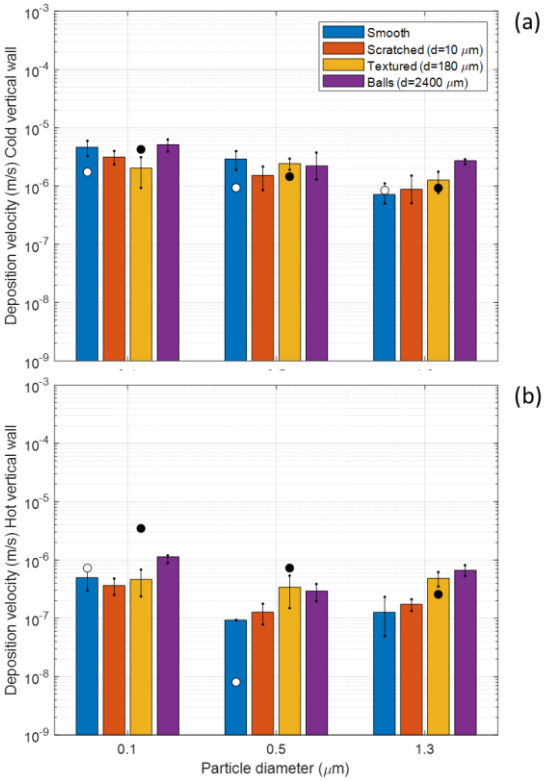


496

497 Figure 10. Deposition velocities on the (a) cold and (b) hot sidewalls.

Finally, we compare the predictions of the present numerical simulations with the experiments of Thatcher and Nazaroff (1997). These authors reported deposition velocities on smooth and rough surfaces installed on the thermally active walls of the cubical cavity sketched in Figure 1. One of the rough surfaces used in the experiments was prepared by lightly scratching smooth cold-rolled stainless steel with a wire grinding brush. The corresponding estimated size of the roughness elements for this scratched surface is about 10 μm. A second surface was a painted aluminum casting of skip-coat texture drywall taken from a residence resulting in a measured roughness height of 180 μm. A third surface was a smooth surface with a mounted array of balls with a diameter of 2400 μm. The corresponding Reynolds numbers ($Re_d$), based on the shear rate on the horizontals walls, for these three surfaces are $2{\cdot}10^{-5}$, $8{\cdot}10^{-3}$ and 1.4, respectively. It can be seen that only the second surface is within the range of Reynolds numbers analyzed (see Table V). Figures 9 and 10 show the measured deposition velocities for three different particle sizes (0.1, 0.5 and 1.3 μm) with bars and the model predictions with circles. Figure 9 corresponds to the horizontal walls (cold ceiling and warm floor) and Figure 10, to the hot and cold sidewalls. The deposition velocities on the horizontal walls have been computed by adding or subtracting the terminal velocity of the particles ($v = k_c \pm V_s$) in the case of the deposition on the floor or on the ceiling, respectively (Pallares and Fabregat, 2020). In these figures we included the measurements of the particle deposition, reported by Thatcher and Nazaroff (1997), on the scratched surface ($d = 10\ \mu m$) and on the surface with balls ($d = 2400\ \mu m$) for comparison purposes. The predictions for smooth surfaces obtained with the model, based on the boundary layer theory, reported by Pallares and Fabregat (2021), are plotted with white circles and the estimates corresponding to the present numerical simulations for $d = 180\ \mu m$ are indicated with black circles.

Figure 9, corresponding to the horizontal walls, shows a larger deposition on the hot floor (Fig. 9b) than in the cold ceiling (Fig. 9a) for the particles with diameters 0.5 μm

and 1.3 μm. The terminal velocities for these particles are $7 \cdot 10^{-6}$ m/s and $6 \cdot 10^{-5}$ m/s. These values are close to the theoretically predicted and measured deposition velocities on the hot wall indicating that the dominant deposition mechanism is gravity. It can be seen that for these particles the measured and the predicted deposition velocities are essentially independent of the rugosity of the surface. For the smallest particles the terminal velocity is $10^{-7}$ m/s and the measured and theoretically predicted deposition velocities are about one order of magnitude larger, $O(10^{-6})$ with larger deposition on the cold ceiling than on the hot floor because of the thermophoretic effect.

The model predicts no deposition on the cold ceiling (Fig. 9a) for the larger particles independently of the rugosity of the wall because the terminal velocity of these particles is larger than the predicted deposition velocities. As for the hot floor, the theoretical prediction of the deposition velocity for the smallest particles is larger for the rough wall than for the smooth surface. However, the measurements do not show a robust trend considering the extension of the error bars.

Figure 10, corresponding to the vertical sidewalls, shows that the deposition velocities are in general larger on the cold (Fig. 10a) wall than on the hot (Fig. 10b) wall, because of the thermophoretic effect. On the cold sidewall the theoretical predictions are in agreement with measurements and indicate that the deposition velocity is larger in the rough surface than in the smooth wall. The boundary layer model predicts a very small deposition or no deposition at all on the smooth cold sidewalls for the particles with diameters of 0.5 μm and 1.3 μm (see Fig. 10b). It can be seen that there is a significant increase of the deposition velocities for the textured rough surface in comparison with the smooth surface, especially for the hot vertical wall.

## 5. CONCLUSIONS

We reported simulations of the particle wall mass transfer rates on heated or cooled rough surfaces. The momentum and the thermal energy equations have been solved

numerically in the vicinity of the wall together with a mass transfer transport equation for the particle concentration. To predict the particle deposition on relatively long rough surfaces we have computed sequentially the mass transfer boundary layer development in a series of unit computational cells with two consecutive two-dimensional square roughness elements. The concentration of particles at the outlet of an upwind unit computational domain is used as the boundary condition at the inlet of the next unit computational cell. Following this strategy, we simulated the particle deposition on rough surfaces with a length corresponding to 2000 roughness heights periodically distributed along the streamwise direction for different flow conditions (Reynolds numbers), temperature increments (thermophoretic effects) and particle diameters (Schmidt number). The particle wall mass transfer rates on rough surfaces increase in comparison with the smooth surfaces specially for large Péclet numbers with typical factors between 3 and 4, for the conditions investigated. When the thermophoretic effect is considered, the particle deposition is enhanced on the cold walls with maximum factors of about 3 for large Péclet numbers while is essentially suppressed on the hot walls. The numerical predictions of the particle deposition velocities have been compared with measurements reported in the literature in a cubical cavity with two pairs of opposed consecutive walls at different temperatures. In general, both predictions and measurements, indicate that the deposition velocities increase for rough surfaces when compared to smooth surfaces, especially for vertical hot walls. On the horizontal walls the effect of the roughness is reduced, with deposition velocities essentially independent of the rugosity of the wall, especially for the large particles.

*Acknowledgements*

This study was funded by the Spanish Ministerio de Ciencia e Innovación through the grants PID2020-113303GB-C21 and RTI2018-100907-A-I00 (MCIU/AEI/FEDER) and by the Generalitat de Catalunya through the grant 2021 SGR 00732.

589

590 **REFERENCES**

591

592 Abadie, M., Limam, K., & Allard, F. (2001). Indoor particle pollution: effect of wall
593 textures on particle deposition. Building and Environment, 36(7), 821-827.

594

595 Allen, M.D., Raabe, O. G. (1982) Re-evaluation of Millikan's oil drop data for the
596 motion of small particles in air, Journal of Aerosol Science, 13(6), 537–547.

597

598 Boccardo, G., Sethi, R., & Marchisio, D. L. (2019). Fine and ultrafine particle deposition
599 in packed-bed catalytic reactors. Chemical Engineering Science, 198, 290-304.

600

601 Chavez R., Orea D., Choi B., Nguyen T. D., Anand N. K., Hassan Y. & Sabharwall P.
602 (2020) An experimental study of solid and liquid aerosol transport in a horizontal
603 square channel, Aerosol Science and Technology, 54:12, 1399-1423.

604

605 Dritselis, C. D. (2017). Numerical study of particle deposition in a turbulent channel
606 flow with transverse roughness elements on one wall. International Journal of
607 Multiphase Flow, 91, 1-18.

608

609 Fabregat, A. and Pallares, J. (2020). Heat transfer and boundary layer analyses of
610 laminar and turbulent natural convection in a cubical cavity with differently heated
611 opposed walls, International Journal of Heat and Mass Transfer, 151, 119409.

612

613 Grau-Bové J., Mazzei L., Thickett D. & Strlič M. (2019) New Perspectives on the study of
614 particulate matter deposition within historic interiors, Studies in Conservation, 64:4,
615 193-202.

616

617 Hahn, L. A., Stukel, J. J., Leong, K. H., & Hopke, P. K. (1985). Turbulent deposition of
618 submicron particles on rough walls. Journal of Aerosol Science, 16(1), 81-86.

619

620

621 Hamdani, S., Limam, K., Abadie, M. O., & Bendou, A. (2008). Deposition of fine
622 particles on building internal surfaces. Atmospheric Environment, 42(39), 8893-8901.
623
624 Hong, W., Wang, B., & Zheng, J. (2020). Numerical study on the influence of fine
625 particle deposition characteristics on wall roughness. Powder Technology, 360, 120-
626 128.
627
628 Inthavong, K. (2020) From indoor exposure to inhaled particle deposition: A
629 multiphase journey of inhaled particles. Experimental and Computational Multiphase
630 Flow 2, 59–78.
631
632 Kalilainen, J., Rantanen, P., Lind, T., Auvinen, A., & Dehbi, A. (2016). Experimental
633 investigation of a turbulent particle-laden flow inside a cubical differentially heated
634 cavity. Journal of Aerosol Science, 100, 73-87.
635
636 Koren, B., A robust upwind discretization method for advection, diffusion and source
637 terms, Technical Report, Centrum voor Wiskunde en Informatica, Department of
638 Numerical Mathematics, Amsterdam, The Netherlands, 1993.
639
640 Kvasnak, W., Ahmadi, G., Bayer, R., & Gaynes, M. (1993). Experimental investigation of
641 dust particle deposition in a turbulent channel flow. Journal of Aerosol Science, 24(6),
642 795-815.
643
644 Lai, A. C. (2002). Particle deposition indoors: a review, Indoor air, 12(4), 211-214.
645
646 Lai, A. C., Byrne, M. A., & Goddard, A. J. (2002). Experimental studies of the effect of
647 rough surfaces and air speed on aerosol deposition in a test chamber. Aerosol Science
648 & Technology, 36(10), 973-982.
649
650 Lai, A. C., Nazaroff, W. W. (2005). Supermicron particle deposition from turbulent
651 chamber flow onto smooth and rough vertical surfaces, Atmospheric Environment,
652 39(27), 4893-4900.

Lévêque M. A. (1928) Les lois de la transmission de chaleur par convection, Ann. Mines Rec. Mem. L'Explotas Mines 13 201–299.

Michaelides, E. (2006) Particles, bubbles & drops: their motion, heat and mass transfer. World Scientific.

Pallares, J. (2015) Local mass transfer rates of a first-order reaction on a wall: Application to the prediction of local platelet deposition in a perfusion chamber, International Journal of Heat and Mass Transfer, 90, 254-258.

Pallares, J. and Grau, F. X. (2010) A modification of a Nusselt number correlation for forced convection in porous media, International Communications in Heat and Mass Transfer, 37 (9) 1187-1190.

Pallares, J., Fabregat, A. (2021) Prediction of particle deposition on the walls of a cubical cavity with differentially heated opposed walls using heat and mass transfer laminar mixed convection boundary layer models, International Journal of Heat and Mass Transfer, 165, 120691.

Pallares, J., Ferré, J. A. (2015) A simple model to predict mass transfer rates and kinetics of biochemical and biomedical Michaelis-Menten surface reactions, International Journal of Heat and Mass Transfer, 80, 192-198.

Pallares, J., Grau, F. X. (2014) Mass transfer rate of a first-order chemical reaction on a wall at high Schmidt numbers, International Journal of Heat and Mass Transfer 69, 438-442.

Shahin, H. I., & Chablani, L. (2023). A comprehensive overview of dry powder inhalers for pulmonary drug delivery: Challenges, advances, optimization techniques, and applications. Journal of Drug Delivery Science and Technology, 104553.

685 Shimada, M., Okuyama, K., Kousaka, Y., & Seinfeld, J. H. (1988). A model calculation of
686 particle deposition onto a rough wall by Brownian and turbulent diffusion. Journal of
687 colloid and interface science, 125(1), 198-211.
688
689 Simard-Normandin, M. Surface Particle Contamination Identification in
690 Microelectronics. In: Particles On Surfaces. CRC Press, 2020. p. 61-76.
691
692 Talbot, L., Cheng, R. K., Schefer, R. W., Willis, D. R. (1980). Thermophoresis of particles
693 in a heated boundary layer. Journal of Fluid Mechanics, 101(4), 737-758.
694
695 Thatcher, T. L., Fairchild, W. A., Nazaroff, W. W. (1996) Particle deposition from natural
696 convection enclosure flow onto smooth surfaces, Aerosol Science and Technology,
697 25(4), 359-374.
698
699 Thatcher, T. L., Nazaroff, W. W. (1997). Effect of small-scale obstructions and surface
700 textures on particle deposition from natural convection flow, Aerosol Science and
701 Technology, 27(6), 709-725.
702
703 Wang, Y., Zhao, Y., & Yao, J. (2019). Large eddy simulation of particle deposition and
704 resuspension in turbulent duct flows. Advanced Powder Technology, 30(3), 656-671.
705
706 Zhao, B., & Wu, J. (2006). Modeling particle deposition onto rough walls in ventilation
707 duct. Atmospheric Environment, 40(36), 6918-6927.
708
709 Zhong, X., Fu, S. C., Chan, K. C., & Chao, C. Y. (2021). Experimental study of particle
710 deposition on patterned microstructured surfaces in a chamber environment. Journal
711 of Aerosol Science, 157, 105802.
712